Synthesis and studying induction heating of $Mn_{1-x}Zn_xFe_2O_4$ (x=0-0.5) magnetic nanoparticles for hyperthermia treatments.

Hussein. S.M [1, a*], T. H. MUBARAK [2, b], S. M. ALI RIDHA [3, c], J. AL-ZANGANAWEE[4, d].

[1] University of Diyala, College of Science, Department of Physics, Iraq.

[2] University of Diyala, College of Science, Department of Physics, Iraq.

[3]University of Kirkuk, College of Education for Pure Science, Department of Physics, Iraq.

[4] University of Diyala, College of Science, Department of Physics, Iraq.

[a]husseinqa83@yahoo.com,[b]dean@sciences.uodiyala.edu.iq,[c]sabahyagmur@yahoo.com, [d]Jasimmansoor13@gmail.com

Keywords: hyperthermia, Nanoparticles, Superparamagnetic, ferrofluids, specific heat.

Abstract

The current development confirms the need for magnetic nanoparticles to treat tumors to become more secure in thermal therapy. Self-regulate magnetic nanoparticles of $MnZnFe_2O_4$ may be proper for thermal treatments. The structure and magnetic properties of the synthesis $Mn_{1-x}Zn_xFe_2O_4$ with x=0-0.5 by step 0.1were studied. Nanoparticles of $MnZnFe_2O_4$ were prepared by the co-precipitation method and followed by heat treatment in an autoclave reactor. XRD results showed that it had been difficult to prepared MnZn-ferrite directly by using the coprecipitation method. FESEM images confirmed that the preparation method produced spherical nanoparticles with a slight change in the particle size distribution, as well as the Particle size has shrunk after the heat treatment. The average particle size has estimated to be about 20 nm. FTIR spectra of samples showed two distinct absorption bands, the band at ~ 617(cm^{-1}) and the ~426 (cm^{-1}) to the tetrahedral and octahedral site respectively were assigned. The absorption bands of the tetrahedral site slightly shifted towards high frequency with increasing Zinc content. According to a magnetic measurement, the study indicates the size of particles is sufficiently small to behave superparamagnetically, the hysteresis loop curves perfectly matched it shows typical soft magnetic materials. The heating ability of water-based colloidal dispersions studied under magnetic field strength 6.5kA/m and the frequency 190 kHz. The results showed that when increasing Zn^{2+} concentration to 0.3 or more temperature of fluids was not raised. Depending on the increase in the heating curve, the susceptibility, effective relaxation time and Néel relaxation time were determined.

1. Introduction

Over the past two decades, scientific interest has focused on the employment and use of magnetic nanoparticles in biomedical applications [1,2,3]. Nanosize magnetic oxides have attracted spacious attention given its flowing applications that range from basic research to industrial applications.

Spinel ferrite, MFe_2O_4 (M=Mn, Co, Zn, Mg, etc.), is one of the most important magnetic oxides, where oxygen has fcc close packing and M^{2+} andFe^{3+} ions can occupy either tetrahedral(A) or octahedral(B) interstitial sites [4]. However, the magnetic properties of nanoparticles strongly depend on various factors such as the synthesis conditions, particle size, shape, and composition. Therefore, the ability to manipulate the shape and size of nanomaterials is critical to determine their magnetic properties and to fulfill scientific and technological needs. Accordingly, it is desirable to develop strategies for the morphology-controlled synthesis of nanosized spinel ferrites [5].Magnetic hyperthermia therapy has currently attracted substantial attention as a safe method for cancer therapy. It can raise the temperature in tumors to 41- 46℃. thereby it could kill the tumor cells with minimal damage to normal tissue. This method includes the introduction of ferromagnetic or superparamagnetic nanoparticles into the tumor tissue, followed by irradiation using an alternating current (AC) magnetic field [6]. Although the Fe_3O_4 MNPs commonly used for hyperthermia applications, however, an increase in the concentration of ferrofluid within the cell may harm normal cells, were the Curie temperature of Fe_3O_4, 858 K, is much higher than the suitable Curie temperature (315-320 K) for the heat generation purposes [7,8]. Therefore, the need for other forms of ferrofluids to be more appropriate for medical applications has been raised. The Perovskite crystal structure of $La_{1-x}Sr_xMnO_3$ (LSMO) have low Curie temperature varied from 283 to 380 K depending on the divalent ion substitution in the composition [9]. Hyperthermia temperature 42–43(℃) has been achieved by using the perovskite structure of superparamagnetic $La_{0.77}Sr_{0.23}MnO_3$ nanoparticles under magnetic fields of 293.3 and 335.3 Oe, and frequency of 267 kHz [10].The change of zinc content controls the Curie temperature in the $Mn_{1-x}Zn_x$ Fe_2O_4 nanoparticles. It had observed that an increase of zinc content for x = 0.5, 0.6, 0.8, and 1 caused a decrease in Curie temperature from 320℃ when x=0.5 to 240℃ at x=1[11]. Thus, the regulation of heat dissipation in hyperthermia treatment becomes possible [12].

The main goal of the research is synthesis $Mn_{1-x}Zn_x$ Fe_2O_4 where x=0-0.5 with a step of 0.1 by using a co-precipitation method and influence of heat treatment by utilizing an autoclave reactor, as well as it has studied the effect of zinc replacement on the structural, magnetic, and heating abilities of fluid samples. However, the use of an alternating magnetic field for clinical applications has faced restrictions because of the eddy currents induced in biological tissue. Experimentally, the criterion value ($f.H < 4.85 \times 10^8$ A/m.s) was considered suitable for clinical applications [13]. In actuality, this critical value has been taking into consideration in the research.

2. Materials and method

2.1. Raw Materials and chemicals

Ferric Chloride III ($FeCl_3$) 98%, Manganese (II) chloride tetrahydrate ($MnCl_2.4H_2O$) 98% AlPHA chemica, Zinc (II) chloride anhydrous $ZnCl_2$98%, Sodium Hydroxide (NaOH) 98% ROMIL pure chemistry, Tetramethylammonium hydroxide ($C_4H_{13}NO$) Merck KGaA. All chemicals were of analytical grade and used as received without further purification.

2.2. Synthesis of $MnZnFe_2O_4$ nanoparticles

MnZn-ferrite nanoparticles of the chemical composition $Mn_{1-x}Zn_xFe_2O_4$ (x = 0, 0.1, 0.2, 0.3, 0.4 and 0.5) were prepared by a chemical co-precipitation method [14]. A stoichiometric amount of $FeCl_3$, $MnCl_2.4H_2O$, and $ZnCl_2$ dissolved in de-ionized water in separate beakers and then transferred to another beaker with continuous stirring to get a homogeneous solution.

Also, 5g of sodium hydroxide was dissolved separately in 100ml de-ionized water. Then, it was added drop-wise into the metal salt solution at room temperature 27-30℃ even pH reaches 12.5 to make sure precipitate all of the metal ions in the solution. Later the solution has heated at 90℃ for one hour with continuous stirring after that turns off and left to cool at room temperature.

Magnetic nanoparticles have been separated and collected via the use of the magnetic decantation method. Then it washed several times with de-ionized water to remove undesirable residual of salts. A small amount of obtained product has dried at 60℃ to study phase composition by XRD analysis, morphology, and size through using FESEM images. In the sodium hydroxide solution with a pH of 13, the rest of the wet product has re-dispersed by stirring the mixture for one hour to be ready for the next step.

To avoid coalescence of adjacent particles mostly happens in the sintering process at high temperature, where the particles in contact with each other. So the second step of preparation was the heat treatment is conducted by the hydrothermal method. The colloidal solution has transferred to the Teflon lined autoclave reactor of 200 ml capacity. The autoclave is sealed and placed in a furnace at 220℃ for 8 hours, then allowed to cool down to room temperature naturally. Then, the colloidal solution will be filtered and washed several times with de-ionized water until neutralized the PH of the discharged solution. Magnetic nanoparticles in the filter paper dried at 60℃.

2.3 Synthesis of ferrofluid

Water-based colloidal nanoparticles had synthesized via the dispersion of 0.5g of $Mn_{1-x}Zn_xFe_2O_4$ nanoparticles in a solution consisting of 8ml distilled water and 2ml of Tetramethylammonium hydroxide (TMAOH) had used as a surfactant. The hydroxide group adsorbed the surface of the nanoparticles, while the $[N(CH_3)_4]^+$ cations provide electrostatic repulsion between nanoparticles [15]. The stabilized colloidal solutions had been obtained throughout the sonication of fluid for 6 hours at a separate period. The generated heat from magnetic nanoparticles in the ferrofluids measured in terms of the specific absorption rate (SAR).

3- Results and Discussion

Structural Characterization of MnZn-ferrite nanoparticles.

3-1 XRD analyzes

X-ray diffraction is a powerful non-destructive technique used to examine the chemical composition and crystallographic structure of materials. The study of crystal structures and characterization of phase contents for the samples have implemented by the use of an X-ray diffractometer (XRD 6000, Shimadzu, Japan) operating at 40 kV and 30 mA with Cu K radiation (1.5406 Å), scan range: 10- 90 (deg) and scan speed: 6 (deg/min). X-ray tests had conducted on the two series of samples included that were prepared by the co-precipitation method and what have acquired after heat treatment.

Identification of crystalline compounds and phases had been accomplished by comparing the X-ray diffraction pattern of samples with JCPDS standard data. Fig.1 illustrates the XRD results of samples had prepared via the co-precipitation method. Starting from x=0, it had noted the formation of single-phase $MnFe_2O_4$ and well-matched with the JCPDS card no-010-0319. As soon as 0.1of zinc ions replaced with manganese ions in the synthesis had observed formation of another structure

in the composition include β-Fe_2O_3, $ZnMnO_3$, MnO_2, $ZnFe_2O_4$, and Q-Fe_2O_3. It seems that $Mn^{2+}$and Zn^{2+} ions participate in formation another structure, this inevitably leads to the conclusion that a significant single-phase of MnZn-ferrite couldn't prepare directly by the co-precipitation route.

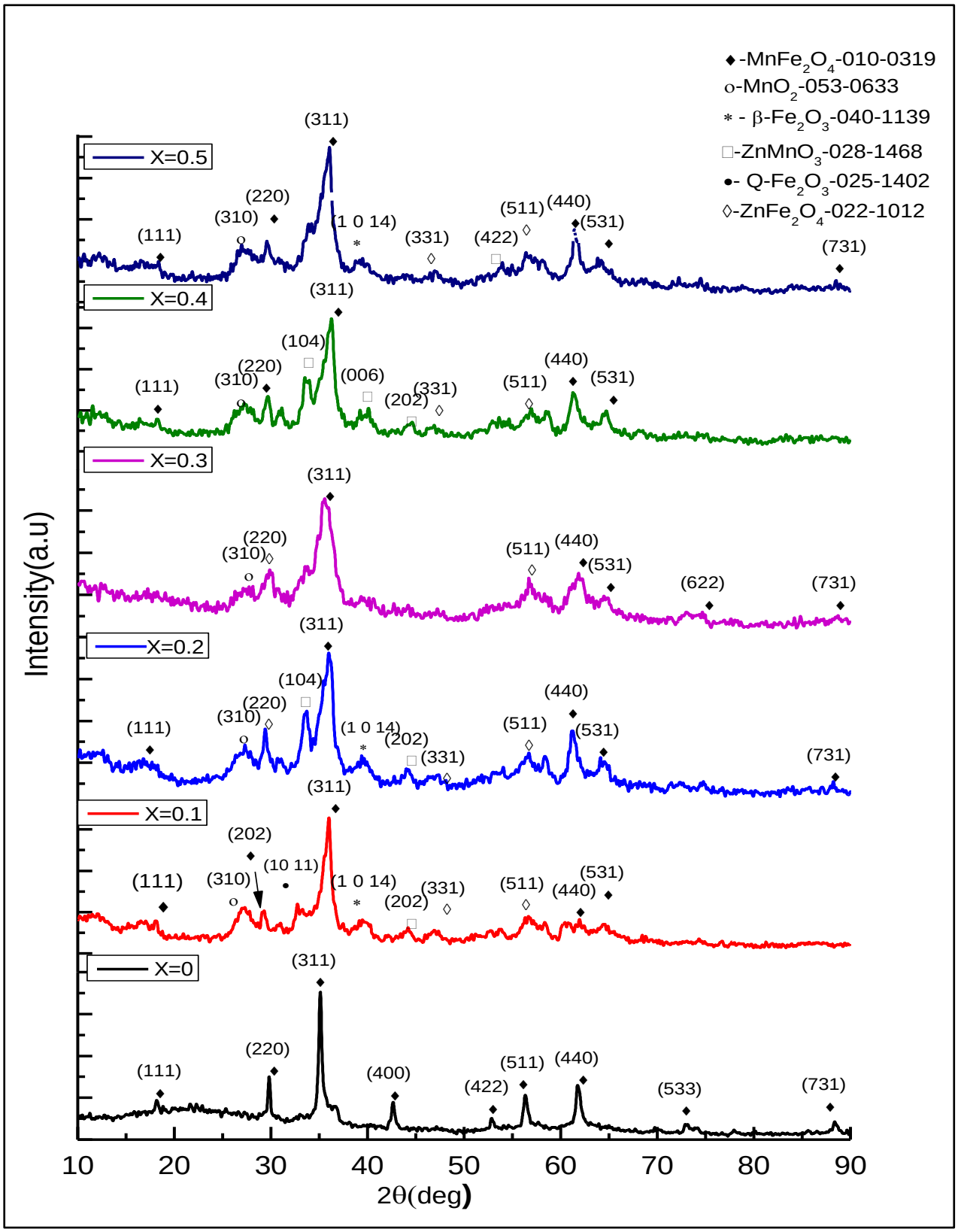

Figure.1. XRD results of the synthesized $Mn_{1-x}Zn_xFe_2O_4$ nanoparticles and the phase composition of prepared samples by co-precipitation method.

The result of samples which have heat-treated by a hydrothermal autoclave reactor had shown a single-phase structure for $Mn_{1-x}Zn_xFe_2O_4$. Most peaks are well-matched with JCPDS standard data of MnZn-ferrite, as shown in Fig.2. It can conclude that $Mn^{2+}$and Zn^{2+} ions are well-substituted in the ferrite structure. Nevertheless, the phase analysis confirmed the presence of Mn_3O_4 in the composition. We are going to choose these samples to complete our study based on XRD results.

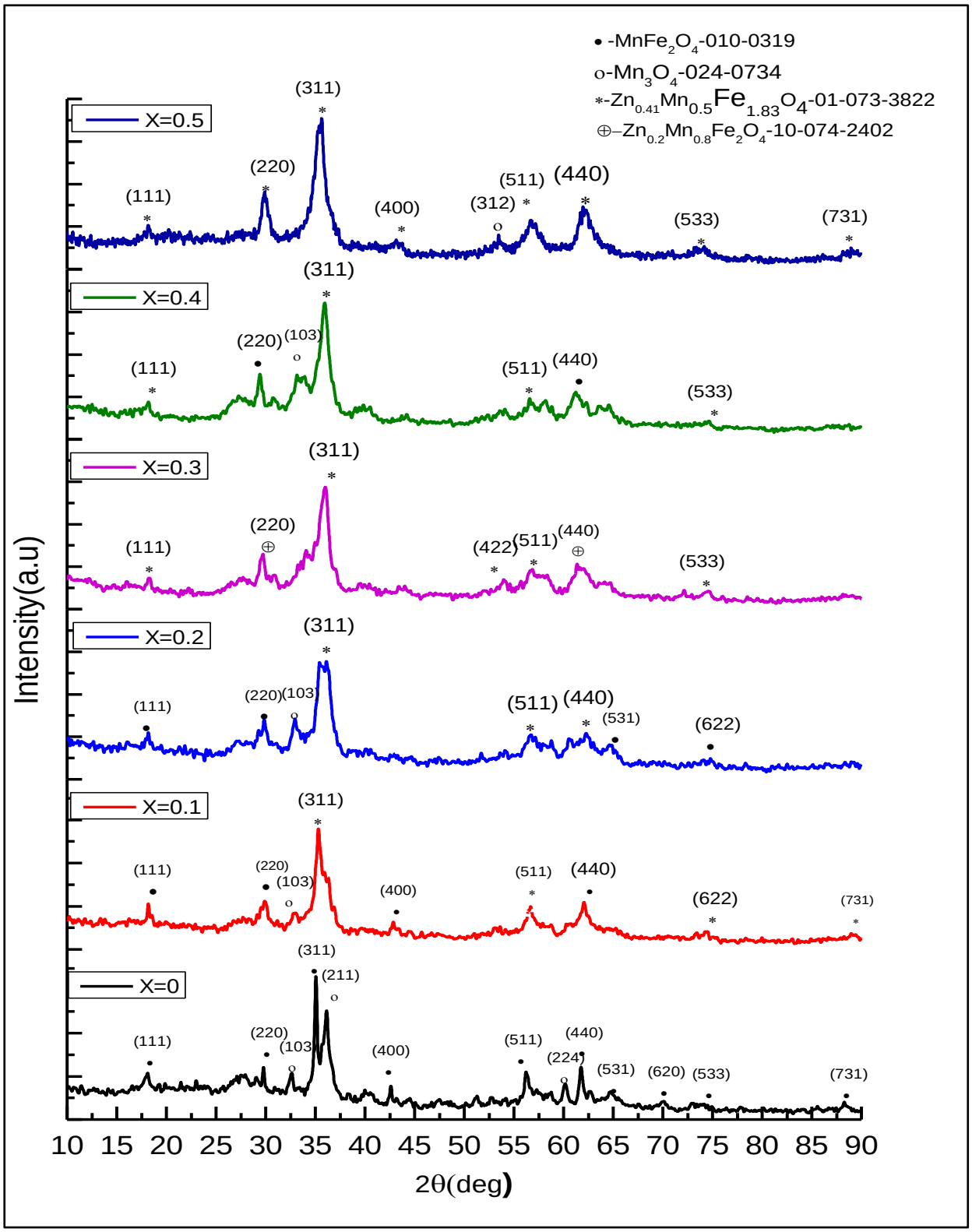

Figure.2, XRD results of the synthesized $Mn_{1-x}ZnxFe_2O_4$ nanoparticles and the phase composition of the samples that have thermally treated in an autoclave reactor.

Lattice constant (a) for the cubic system calculated by using the following equation:

$$a_{exp} = d_{hkl}\sqrt{h^2 + k^2 + l^2} \quad (1)$$

Where, d_{hkl} – inter planer distance, h, k, l – Miller indices. The X-ray density (ρ_x) is dependent on the molar mass of the synthesized compound and the lattice parameter (a_{exp}) calculated by using the relation:

$$\rho_x = \frac{z\,M}{N_A\,V} \quad (2)$$

Z- Is the number of molecules per formula unit (Z = 8 for spinel system), M is the molecular mass of the sample, $V=a_{exp}^3$ is the unit cell volume of the cubic structure, N_A- is the Avogadro's number equals 6.023×10^{23} (atom/mole) [16]. The average crystallite size determined from the broadening of the XRD pattern. According to Scherrer's equation:

$$D_{ave} = K\lambda/\beta\cos\theta \quad (3)$$

Where D is the average crystallite size, λ is the X-ray wavelength, θ is the Bragg angle, and β is the finite size broadening and K is the shape factor (K =0.94) for spherical crystallites with cubic symmetry [17].

Structural formula of $MnFe_2O_4$ is mixed spinel structure where the bivalent cations (Me^{2+} = Mn^{2+}) are distributed on both tetrahedral and octahedral sites. Structural formula of such ferrites is $Me_{1-\delta}^{2+}Fe_{\delta}^{3+}\left[Me_{\delta}^{2+}Fe_{2-\delta}^{3+}\right]O_4^{2-}$, where δ is the inversion degree = 0.2 for Manganese ferrite [18]. The zinc ferrite has a normal spinal structure and zinc ions occupying the tetrahedral site preferentially, the observed magnetic moment of zinc ferrite has paramagnetic value [19]. Given that the Zn^{2+} ions occupy the A-sites preferentially, while the Fe^{3+} and Mn^{2+} ions are distributed among the A and B-sites. The distribution of cations and structural parameters is strongly dependent on the synthesis method and annealing temperature [20]. The cation distribution of $Mn_{1-x}Zn_xFe_2O_4$ represented as:$(Zn_x\,Mn_{0.8-x}^{2+}\,Fe_{0.2}^{3+})_A[Mn_{0.2}^{2+}\,Fe_{1.8}^{3+}]_BO_4^{2-}$, where A and B designate the tetrahedral and octahedral sites respectively. Based on the proposed cation distribution of $Mn_{1-x}Zn_xFe_2O_4$, the average cationic radius at A and B -sites have been calculated using the expressions given below:

$$r_A = c(Zn_A^{2+}).\,r(Zn_A^{2+}) + c(Fe_A^{3+}).\,r(Fe_A^{3+}) + c(Mn_A^{2+}).\,r(Mn_A^{2+})$$

$$r_B = \frac{1}{2}[c(Fe_B^{3+}).\,r(Fe_B^{3+}) + c(Mn_B^{2+}).\,r(Mn_B^{2+})]$$

Where c is the ionic concentration at the tetrahedral and octahedral sites, r(Å) is the ionic radii for substituted ions in A-site; $r\left(Zn_A^{2+} = 0.6Å\right), r\left(Fe_A^{3+} = 0.49Å\right), r\left(Mn_A^{2+} = 0.66Å\right)$ furthermore, the ionic radii for the cations in B-site; $r\left(Zn_B^{2+} = 0.74Å\right), r\left(Fe_B^{3+} = 0.645Å\right), r\left(Mn_B^{2+} = 0.83Å\right)$ were taken from Shanon [21].Using the ionic radii of A-site (r_A) and B-site (r_B); the theoretical lattice constant (a_{th}), can be calculated by the relation:

$$a_{th} = \frac{8}{3\sqrt{3}}\left[(r_A + R_0) + (\sqrt{3}(r_B + R_0)\right] \quad (4)$$

Where R_o is the ionic radius of oxygen ion = 1.38Å [22]. The theoretical lattice parameters have summarized in Table1.

The lattice parameter decreases with the increase of zinc content(x) and nearly amount to their theoretical values, except at sample x = 0.5 as given in Table1. The decreases in the lattice parameter happened due to the replacement of zinc ions with manganese ions in the structure. Whether the zinc ions substituted in the tetrahedral or octahedral sites it causes decreases in the lattice parameter because of Zn^{2+} ions has a smaller ionic radius than Mn^{2+} ions. The increase of lattice constant when x=0.5 is probably due to the replacement of Zn^{2+} ions with Fe^{3+} ions in the tetrahedral site, evidenced by the appearance of relatively high intensity in the peak reflection from the plane (220) as noted in Fig.2. X-rays reflection of a plane (220) occurring as a result of the reflection from the localized atoms at the tetrahedral sites in the spinel structure [23].

The theoretical density obtained from x-ray measurements increased by increasing zinc content in the structure but differed for x=0.5 because the increase in the lattice constant caused the growth of the crystal size leads to a decrease in density. Can be seen in Fig.2 the peaks broadening increased gradually with an increase of zinc content in the structure as a result of crystallite size decrease, it was calculated by Scherrer's equation (Eq.3) as shown in Table1.

The distance between the tetrahedral cation and anion known as tetrahedral bond length d_{A-O} and the distance between the octahedral cation and anion known as octahedral bond length $d_{B\text{-}O}$, calculated by using the expressions were calculated by using the expressions [24]:

Tetra-O separation A-O $$d_{A-O} = a\sqrt{3}\,(u - 0.25) \quad (5a)$$

Octa-O separation B-O $$d_{B-O} = a[3u^2 - 2.75u + \tfrac{43}{64}]^{\frac{1}{2}} \quad (5b)$$

Oxygen positional parameter (u) is the distance between an oxygen ion and a face of a cube. The ideal FCC, parameter is u = 3/8 = 0.375 for an ideal close-packed arrangement of O atoms. The anion parameter (u) calculated by using the expression:

$$u = \left(\frac{(r_A + R_0)}{\sqrt{3} * a_{exp}} + ¼\right) \quad (6)$$

For the unit-cell origin at A-site, where, r_A = ionic radii of A-site, R_o = 0.138 (nm) ionic radius of oxygen ion and a_{exp} is the experimental lattice parameter [25]. The approximate value of the oxygen positional parameter (u) has taken depending on theoretical value of r_A.

In spinel structure, the packing of the ions within the lattice is perfect when oxygen parameter u =0.375. However, anions in spinel structures usually are deviated from their ideal position. Therefore, the parameter δ represents the deviation from the typical value determined by the relation$\delta = u - 0.375$. The results of the calculation of oxygen positional parameter, and inversion parameter δ for MnZn-ferrite are presented in Table1. The value of u for the studied samples increases from 0.3865 to 0.387 in going from x = 0 to 0.2, then it will decrease to 0.385 at x=0.5, the inversion parameter changes accordingly. It is obvious that u parameter increases with increases Zn content may be due to the shift of the origin at the tetrahedral sites with replacement of Zn^{2+} ions with Mn^{2+} ions, then the deviation decreases when Zn^{2+} ions been replaced with Fe^{3+} ions, it demonstrated based on decreasing in the tetrahedral bond length.

The jump length or hopping length (L) is the distance between two magnetic ions such as Tetra-tetra A-A (A), Octa-octa B-B [B], and Tetra-octa A-B. The hopping length had calculated by using the following relations [26]:

$$L_{A-A} = (a_{exp}\sqrt{3})/4 \quad (7a)$$

$$L_{B-B} = (a_{exp}\sqrt{2})/4 \quad (7b)$$

$$L_{A-B} = (a_{exp}\sqrt{11})/8 \quad (7c)$$

Interionic distances between cations (A-A), (A-B), and (B-B) for the $Mn_{1-x}Zn_xFe_2O_4$ ferrite system decrease with an increase in the zinc content, it can be understood by the fact that an element with higher ionic radius Mn^{2+} is replaced by an ionic with lower ionic radius Zn^{2+}, but for the sample x=0.5, Zn^{2+} my replaced by Fe^{3+} ions, so the hopping lengths increased. The results of the calculation all preceding parameters were summarized in the Table1:

Table1: Crystallographic parameters for $Mn_{1-x}Zn_xFe_2O_4$ nanoparticles.

(x)	Lattice constant (Å)		X-ray density	average crystallite size	oxygen parameters		bond length(Å)		hopping length 'L' (Å)		
	a_{th}	a_{exp}	$\rho_{x(\frac{g}{cm^3})}$	D_{ave}(nm)	u	δ	d_{A-O}	d_{B-O}	L_{A-A}	L_{B-B}	L_{A-B}
0.0	8.537	8.48	5.02	17.8	0.3865	0.0115	2.004	2.027	3.671	2.998	3.515
0.1	8.528	8.43	5.22	13.5	0.3869	0.0119	1.998	2.012	3.650	2.980	3.494
0.2	8.519	8.40	5.41	11.2	0.3870	0.012	1.993	2.004	3.637	2.9698	3.482
0.3	8.51	8.398	5.43	10.5	0.3866	0.0116	1.986	2.006	3.636	2.9691	3.481
0.4	8.50	8.38	5.47	9.3	0.3865	0.0115	1.981	2.003	3.628	2.962	3.474
0.5	8.49	8.44	5.30	7.8	0.3850	0.01	1.973	2.029	3.654	2.983	3.499

3.2-FE-SEM image analysis

Particle size and morphology of $Mn_{1-x}Zn_xFe_2O_4$ samples analyzed using FE-SEM techniques. Fig.3 showed a series of FESEM images which had obtained by the co-precipitation method, and Fig.4 showed a series of FESEM images after heat treatment by hydrothermal autoclave reactor. From FE-SEM images in Fig.3 and Fig.4, it appears that the particles have a spherical shape. Histograms of the particle size distributions carried out by image J software. It confirmed that there is a slight change in the particle size distribution as illustrated in Fig.5, it demonstrates that the particles somewhat are larger before the heat treatment and aggregated. It seems that particles separated by the effect of high pressures and temperatures in the autoclave reactor. Aside from that, the particle size has shrunk after heat treatment. The histograms of the particle size distributions for samples clarify that it tends to be smaller in size after heat treatment. The average particle size is 20 nm.

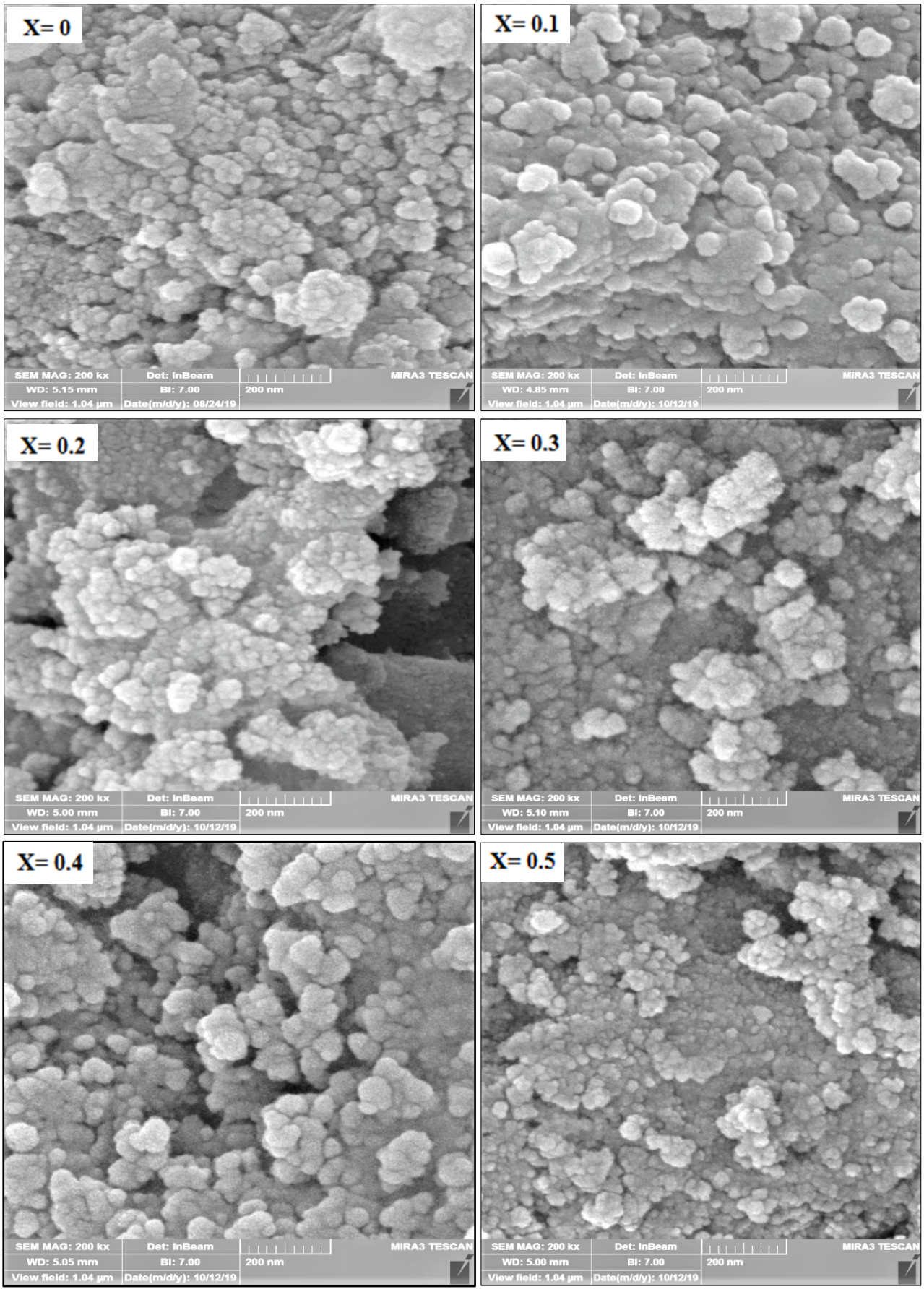

Figure.3. FE-SEM images of $Mn_{1-x}Zn_xFe_2O_4$ nanoparticles that have been prepared by co-precipitation method.

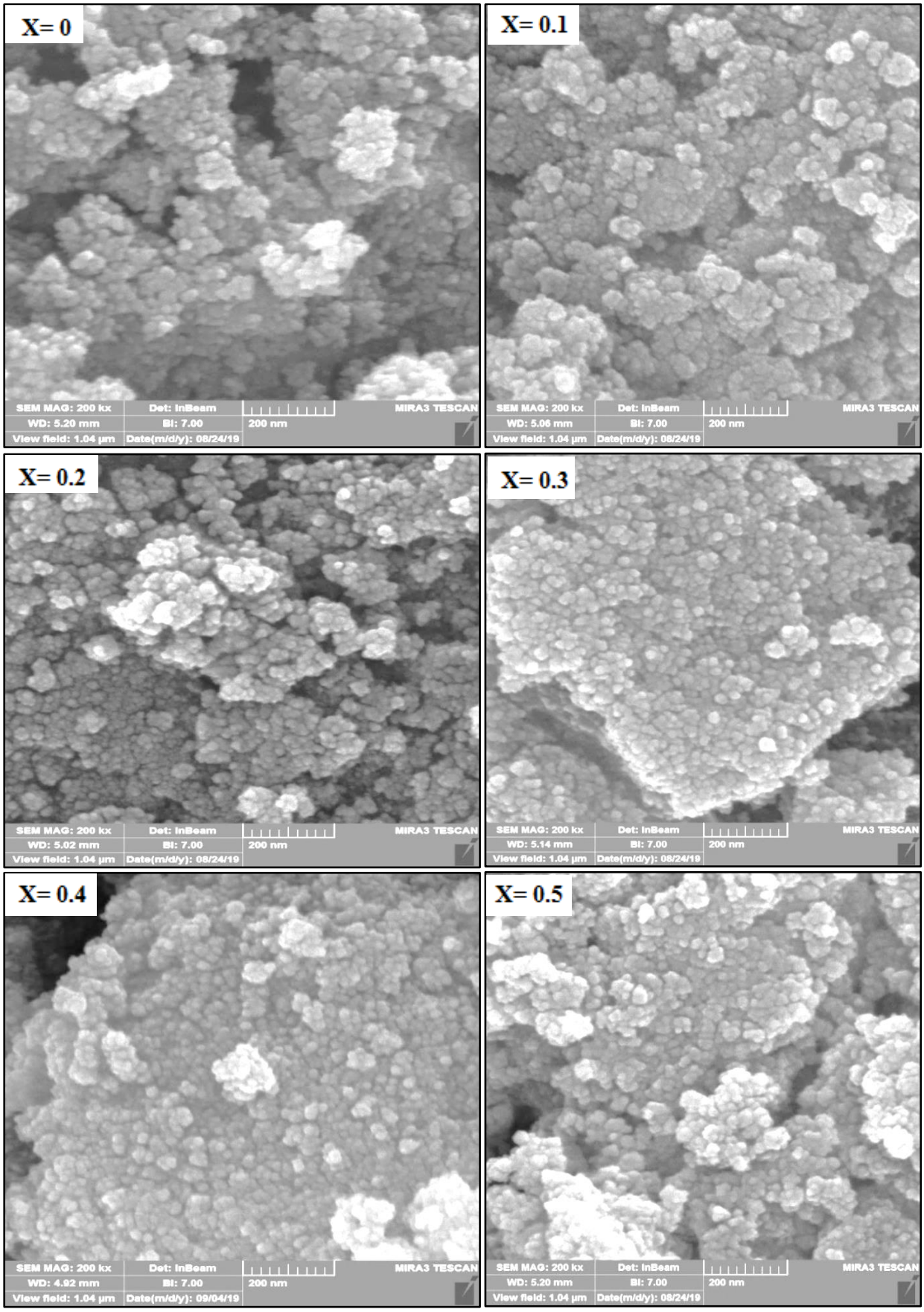

Figure.4. FE-SEM images for $Mn_{1-x}Zn_xFe_2O_4$ nanoparticles that have been thermally treated in autoclave reactor.

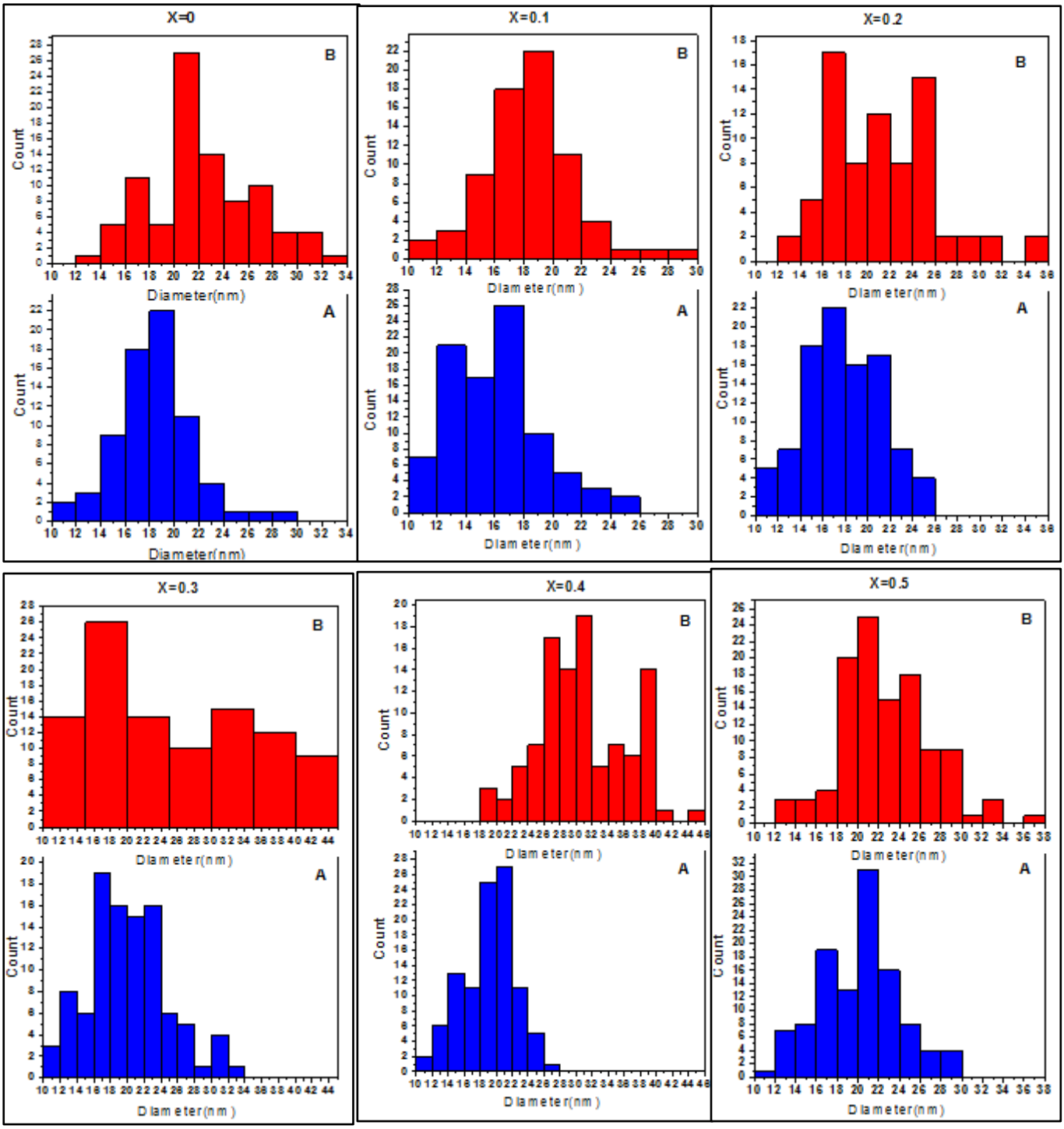

Figure.5.Histograms showing the particle size distributions of $Mn_{1-x}Zn_xFe_2O_4$ nanoparticles, where the letter B- refers to the obtained nanoparticles by co-precipitation method and letter A- refer to nanoparticles size distributions after heat treatment in an autoclave reactor.

3.3-FT-IR spectroscopy analysis

Fourier transform infrared spectroscopy (FTIR) is a powerful tool for identifying different types of chemical bonds present in a molecule by producing an infrared absorption spectrum as a molecular "fingerprint". The wavelength of infrared absorbed is a characteristic of the chemical

bond. Molecular bonds vibrate at various frequencies depending on the type of bonds and elements present [27].

IR spectra were recorded on a spectrophotometer (Shimadzu, IRAffinity-1) in the range 300 - 4000 cm^{-1} by using KBr pellets. Structural investigation and cations redistribution between octahedral and tetrahedral sites deduce by FTIR measurements. The absorption bands within the range of 300 to 700 cm^{-1} attributed to fundamental vibrations of the ions of the crystal lattice [28]. IR spectrum measurements of the Mn_{1-x} $Zn_xFe_2O_4$ showed in Fig.6a. It demonstrates absorption bands lie within the region ~625 to ~350 cm-1 with existence splitting or shoulders in the absorption bands.

Peak position for Fe-O bond among splitting bands designated as shown in the Fig.6b, based on the ion radius in tetrahedral and octahedral sites. As well as, the wavenumber is inversely proportional to the bond length. The ionic radius for situated cations at A-sites is smaller than B-site will make the bond length in A-site is shorter than B-site. Therefore the bonds at A-sites vibrate faster.

The peak position for Fe-O bond in the B-site specified among the splitting band in the absorption bands depending on Waldron supposed i.e. $v_1/v_2 \approx \sqrt{2}$ [28]. The force constant for A-sites are nearly equal to force constant for B-sites even as A- sites have four coordination number while B-sites have six coordination number [29]. The force constant of the tetrahedral site (K_T) and octahedral site (K_O) determined by using the equation $K= 4\pi^2c^2v^2\mu$ [30]; can be rewritten as:

$$K\left(\frac{\text{dyne}}{\text{cm}}\right) = 58.98 \times 10^{-3} * (v_{(cm^{-1})})^2 * \mu(\text{amu}) \qquad (8)$$

Where μ is the reduced mass and given by $\mu = \frac{m_1 * m_2}{m_1 + m_2}$, m_1 is the atomic mass of the cations residing at the A-site or B-site, m_2 is the atomic mass of oxygen anion. The force constant and the absorption bands it was listed in Table 2.

Table 2 :IR absorption bands and force constants of the $Mn_{1-x}Zn_xFe_2O_4$ samples.

(x)	v_1(cm^{-1})	v_2(cm^{-1})	$K_T \times 10^5$ (dynes/cm)	$K_O \times 10^5$ (dynes/cm)	v_1/v_2
0.0	590.21	430.21	2.555	1.357	1.37
0.1	592.14	426.268	2.571	1.332	1.389
0.2	597.93	443.62	2.622	1.443	1.347
0.3	605.64	441.69	2.690	1.430	1.37
0.4	617.22	439.77	2.794	1.418	1.40
0.5	569	437.84	2.374	1.406	1.29

Since the vibrational frequency is proportional to the bond length, the bond lengths in A-site have been listed in Table1 as a function of the zinc content could be built upon. When Zn content increased in going from x=0 to 0.4, the wavenumber of the first band increased, it may be explained

depending on the ionic radius in A-site. When Zn content increased in going from x=0 to 0.4, the wavenumber of the first band increased, it may be explained depending on the ionic radius in A-site. The ionic radius of Mn^{2+} (0.66Å) replaced with Zn^{2+} (0.6Å) caused a shortening of the bond length, so the wave number increased. When increased x to 0.5, the wavenumber decreases may be due to the replacement of Fe ions in A-site with zinc ions lead to increase in the reduced mass, hence the wavenumber decreases($v_1 \propto \frac{1}{\sqrt{\mu}}$). The reduced mass (μ) for the bonds Zn-O, Fe-O and Mn-O equal to 12.85, 12.43 and 12.39 (amu) respectively.

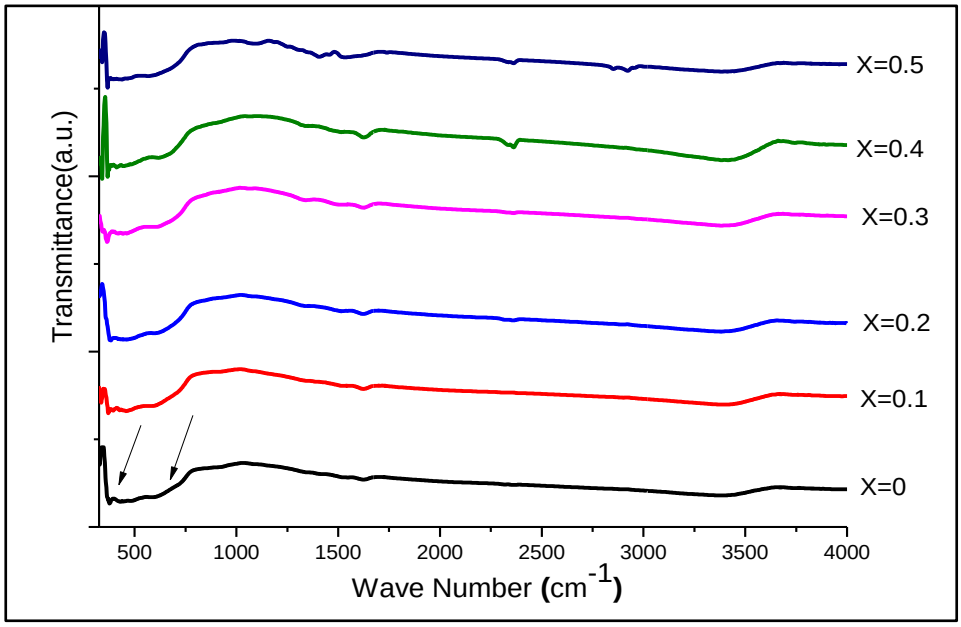

Figure.6a, FTIR spectra illustrate the absorption bands of $Mn_{1-x}Zn_xFe_2O_4$ nanoparticle.

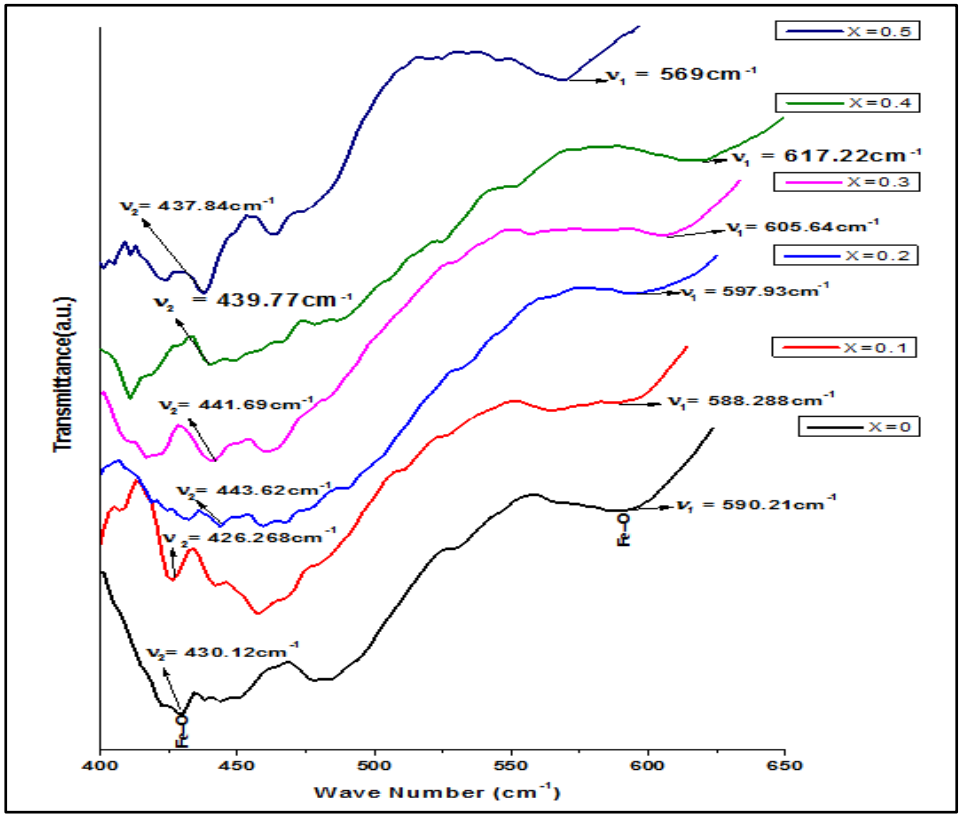

Figure.6b, identifying and analyzing the characteristics of the absorbance band for $Mn_{1-x}Zn_xFe_2O_4$ nanoparticles.

4-Magnetic Properties

Hysteresis Loop measurements were determined using a vibrating sample magnetometer (VSM) at room temperature (300 K). Hysteresis loop curves for $Mn_{1-x}Zn_xFe_2O_4$ serious had shown in Fig.7a, "S" shaped curves that reveal typical soft magnetic material and magnetic coercivity almost neglected. Moreover, particles are so small to behave like superparamagnetic material, where the magnetic moments within the nanoparticle tend to align with each other in a particular direction. It is called easy axes above blocking temperature [31,32].

According to Neel's theory, the total magnetic moment depends on the cations distribution among A and B sites in spinel ferrite [33]. The values of saturation magnetization (Ms), magnetic coercivity (Hc) and remnant magnetization (Mr) had determined from hysteresis loop curves. The magnetic moment per formula unit in Bohr magneton (μ_B) obtained from the following equation [34]:

$$n_B(\mu_B/\text{atom}) = \frac{\text{M.Wt}(\frac{g}{mol})\times M_s(\frac{emu}{g})}{5585} \quad (9)$$

Magneto-crystalline anisotropy constant (K_1) evaluated using the law of approach to saturation (LAS) that derived from hysteresis loop at high magnetic field strengths i.e. $H >> H_C$ in particular, at high magnetic fields corresponding to the saturation magnetization (M_s) is given by the relation:

$$M = M_S\,(1 - \frac{b}{H^2}) \quad (10)$$

Anisotropic constant K_1 for isotropic cubic is calculated by the equation:

$$K_1 = M_s\sqrt{\frac{105\ b}{8}} \quad (11)$$

Parameter b originates from the magneto-crystalline anisotropy. It can be obtained from the Eq.10 by a plot of M versus1/H^2at high magnetic field strengths 3.6- 8(KOe), curve fitting yield a straight line as shown in Fig.7b, intercept of the straight line represents the value of Ms and the slope = Ms.b [35 ,36 ,37].

Effect of chemical composition on magnetic behavior has been provided both by M-H curves and their derivative curves. The variance of the saturation magnetization (M_S) values for samples had obtained from hysteresis loops curves were presented in Table 3. The Ms value decreased from 11.85(emu/g) for x=0 to 5.43 (emu/g), as 0.1 of Zn^{2+} ions is replaced with Mn^{2+} ions in the structure, then it diminish to 0.77(emu/g) at x=0.2, as well equals 1.08(emu/g),when x=0.4.Experimentally observed variation of magnetic moment with zinc content increases, the relative number of ferric or manganese ions on the A-site diminish. This causes a reduction in the A-B interaction. The ionic moments on the B-sites are no longer held parallel to one another and angles between them begin to form, reducing the moment of the B sub lattice itself [19].

However, there is an increase in Ms value at x=0.3and 0.5. It is probably due to the replacement of zinc ions with cations in the B-sites. The observed values of the coercive field (Hc) and remnant magnetization (Mr) are so small, as illustrated in fig.7a, which indicates that the particle size does not exceed the critical diameter of single-domain particles. The net magnetic moments and

magnetocrystalline anisotropy are greatly affected by cation distribution. Magnetic parameters have listed in table 3.

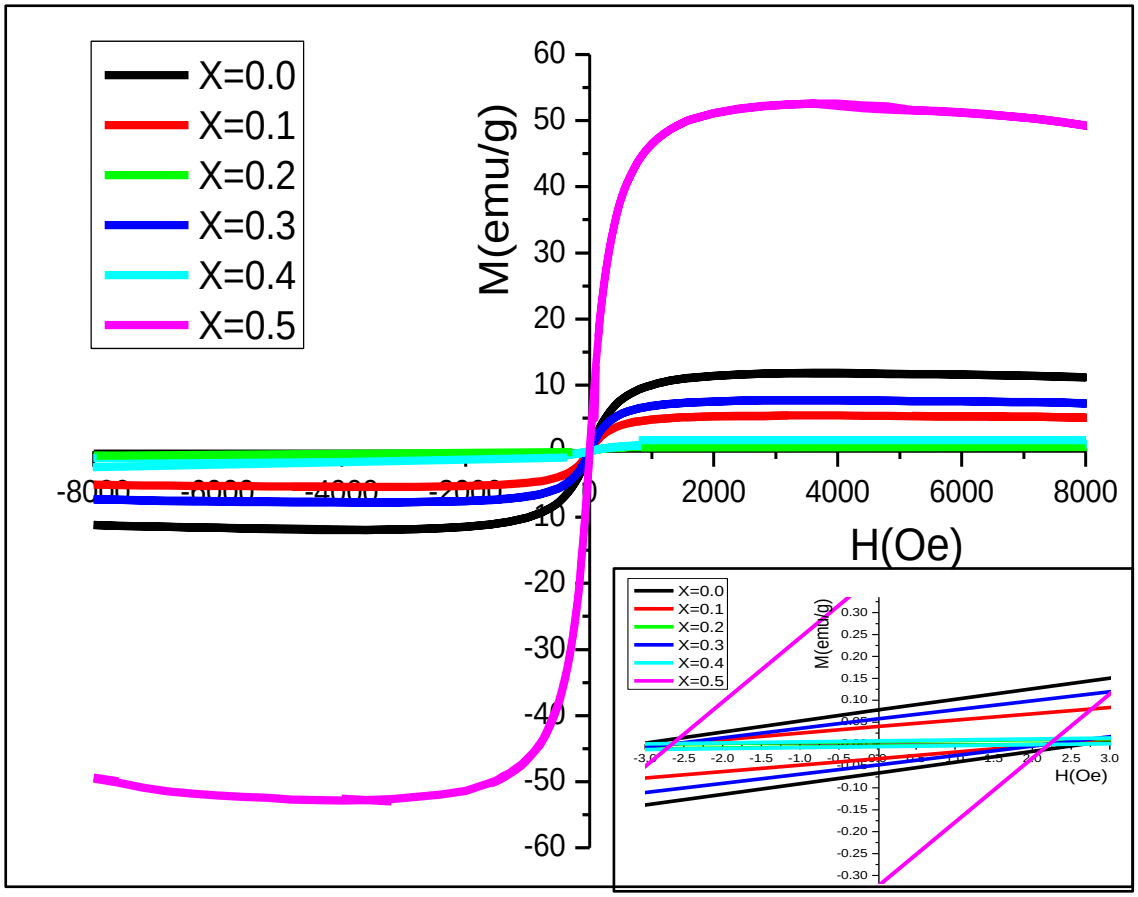

Figure.7a: Magnetization versus applied magnetic field of $Mn_{1-x}Zn_xFe_2O_4$ nanoparticles at 300K.

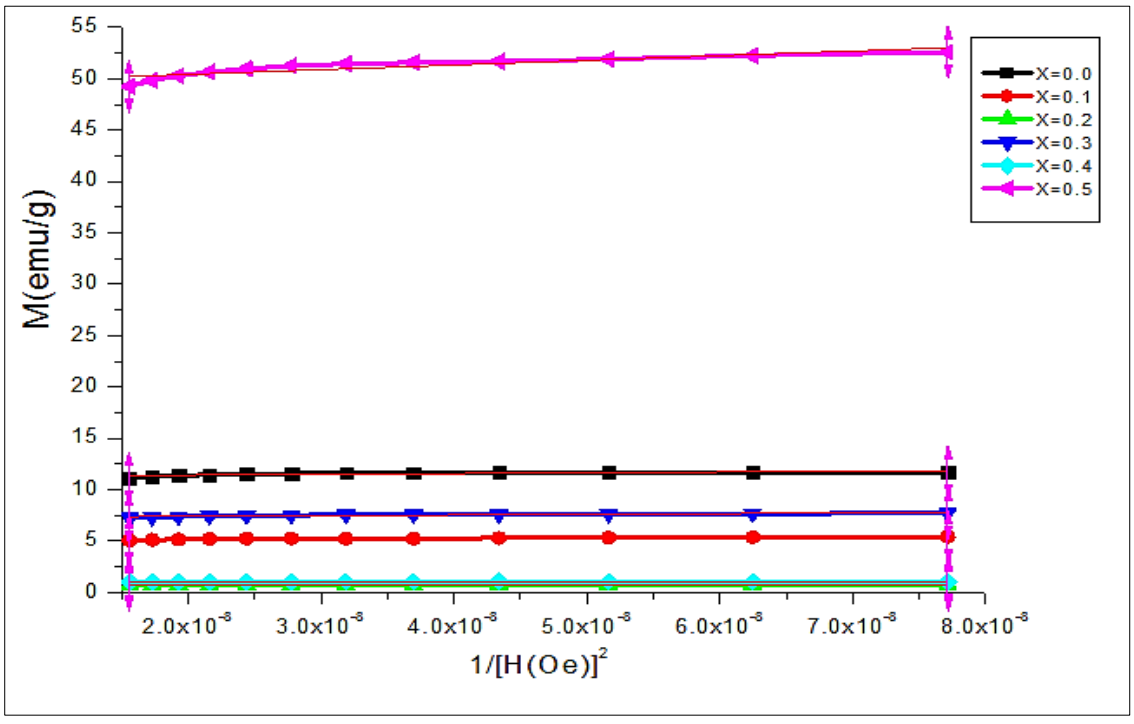

Figure.7b: Magnetization as a function of $1/H^2$ of $Mn_{1-x}Zn_xFe_2O_4$ nanoparticles. The solid lines indicate a linear relation between the magnetization and $1/H^2$ in the field region 3.6-8 kOe.

Table-3: Variation of magnetic parameters for $Mn_{1-x}Zn_xFe_2O_4$ nanoparticles as a function of the zinc content.

(x)	M_S(emu/g)	Mr(emu/g)	H_c(Oe)	K_1(KJ/m^3)	n_B (μ_B/unit cell)
0.0	11.85	0.078	3	18.8	3.91
0.1	5.43	0.04	2.9	9.97	1.8
0.2	0.77	0.005	2.6	1.44	0.25
0.3	7.76	0.06	2.68	14.6	2.6
0.4	1.08	0.008	2.35	1.76	0.36
0.5	52.82	0.35	2.5	97.2	17.84

5-Heat Generation Measurement

Utilize of magnetic nanoparticle in the form of ferrofluids as heat mediators for medical treatments defines Magnetic Fluid Hyperthermia (MFH) [38]. The heating mechanism performed by applying an external alternate magnetic field with proper frequency(f) and amplitude(H), under an alternate magnetic field, the MNPs continuously convert the electromagnetic energy into heat energy [39]. The heat generated from superparamagnetic nanoparticle was described by Rosensweig so-called linear response theory, which states the heat generated by the magnetic nanoparticles is proportional to the imaginary part of magnetic susceptibility (x''). The power dissipation(P) expressed in the following formula:

$$P = \pi\mu_\circ f H^2 x'' \qquad (12)$$

Magnetic susceptibility χ is the magnetization M to the field H when subjected to alternating magnetic field has been described by the Debye model:

$$\chi = \frac{x_\circ}{1+j(2\pi f\tau)} = \chi' + j\chi'' \qquad (13)$$

Where χ' is the real part of magnetic susceptibility, magnetic moments fluctuates in the phase with the alternating magnetic field, while χ'' - phase delay converted into heat energy. The real $\chi'$and imaginary part of magnetic susceptibility χ''given by the relations:

$$x' = \frac{x_\circ}{1+(2\pi f\tau)^2} \quad (14a), \qquad x'' = x_\circ \frac{2\pi f\tau}{1+(2\pi f\tau)^2} \quad (14b), \qquad x_\circ = \frac{\mu_\circ M_S^2 V}{3KT} \quad (14c)$$

Where $x_\circ$ is the initial susceptibility in low-field limit [40,41], and M_s is the saturation magnetization of superparamagnetic NPs equalsφM_d^2, where φ is the volume fraction, M_d the domain magnetization of a suspended particle almost equal to saturation magnetization of the bulk [42]. K is the Boltzmann constant equals1.38 x 10^{-23}J/K, and T the absolute temperature (K) and V is the particle volume.

The relaxation time constant(τ) of superparamagnetic NPs involves two different thermal relaxation mechanisms; Brownian relaxation(τ_B) in which the nanoparticles rotate and cause heating due to shear stresses between particle and surrounding fluid and given by equation [43]:

$$\tau_B = \frac{3\eta\, V_H}{K_B\, T} \qquad (15)$$

Where η is the dynamic viscosity of water at 40℃ equals 6.52×10^{-4} kg / (m·s) [44].$V_H = \frac{\pi}{6} d^3$ is the hydrodynamic particle volume of a spherical particle with the diameter d it estimated from FESEM images equals 20nm. k_B is Boltzmann's constant, T is the absolute temperature equals 313K, had considered compatible with hyperthermia.

Ne´el relaxation(τ_N) in which the magnetic moment rotates with respect to the crystal. Under applied magnetic field Néel relaxation time given by the following expression:

$$\tau_N = \tau_A\left(\frac{\sqrt{\pi}}{2}\right)\left(\sqrt{\frac{K_B T}{KV_M - HM\cos\theta}}\right)\, e^{\frac{(KV_M - HM\cos\theta)}{K_B T}} \qquad (16)$$

Where τ_A- is the attempt frequency generally taken to be 10^{-9} s, and V_M -is the magnetic volume, K- is the anisotropy constant includes all contributions to the anisotropy, k_BT -is the thermal energy, where θ is the angle between the magnetisation and the applied magnetic field [45].

The effective relaxation time (τ) arises from the contributions of both relaxation times of two mechanisms τ_N and τ_B given by the equation [40]:

$$\tau = \frac{\tau_B \cdot \tau_N}{\tau_B + \tau_N} \qquad (17)$$

5.1-Specific Absorption Rate (SAR)

Specific Absorption Rate (SAR) is a measure that indicates the power released by MNPs when subject to an alternating magnetic field. The quantity represents the power per unit mass, expressed in W/g, and can be obtained through the following equation:

$$SAR = \frac{P}{m_{MNP_S}} = \frac{\sum_i m_i\, C_i}{m_{MNP_S}} \frac{\Delta T}{\Delta t} \qquad (18)$$

Where m_i and C_i are mass and specific heat of the i-th specie composing the sample, m_{MNPs} is the total MNPs mass and ΔT is the temperature increase in the interval Δt during which the AC field is on [46].

A measurement of the heating rate during applied of an alternating magnetic field yield a linear function through the adiabatic process. However, the process is non-adiabatic due to heat losses to the environment which increases by the temperature difference between the sample and the surrounding. So the heating curve had measured by Box- Lucas equation:

$$T(t) = A(1 - e^{-Bt}) \qquad (19)$$

Where A is the saturation temperature, B is a parameter related to the curvature of the heating curve. The product of the fitting parameters A×B is equivalent to the initial heating rate i.e. $\frac{\Delta T}{\Delta t}$. The SAR had calculated from the corrected heating curve [47].

5.2- Specific Heat of Nanofluids

The specific heat is one of the prominent properties and plays a significant role in influencing the heat transfer rate of nanofluids. Specific heat of nanofluids $C_{p,nf}$ can be described by the following expression:

$$C_{p.nf} = \frac{\varphi\,(\rho C_P)_n + (1-\varphi)(\rho C_P)_f}{\varphi\rho_n + (1-\varphi)\rho_f} \qquad (20)$$

Assuming that the base fluid and the nanoparticles are in thermal equilibrium, where ρ is the density, C_P is a specific heat and the subscript n,f - refers to the nanoparticle and fluid respectively[48]. The specific heat of water = 4.186 J/g.℃ , also the nanoparticle volume fraction φ defined as follows:

$$\varphi = \frac{m_n/\rho_n}{m_n/\rho_n + m_{H_2O}/\rho_{H_2O}} \qquad (21)$$

Were m_n - nanoparticle mass, ρ_n – density, m_{H_2O}- water mass, ρ_{H_2O}- density of water (1 g/cm^3) [49,50].

Heating ability of 50 (mg/ml) water-based ferrofluids for $Mn_{1-x}Zn_xFe_2O_4$ samples had achieved under magnetic field strength 6.5kA/m and frequency 190 kHz. The heating curves had represented in Fig.8. From the observed heating rate, it was noted the temperature increased in the samples x= 0, 0.1, and 0.2, but it not changed in the x=0.3, 0.4and 0.5, that's because of zinc addition causes decreases in the Curie temperature where the magnitude of the crystal anisotropy generally decreases with temperature more rapidly than the magnetization and vanishes at the Curie point [24]. The heat released from the superparamagnetic nanoparticles occurs by two different relaxation mechanisms, which are Néel relaxation time and Brownian relaxation time [40]. The heat produced by the Brownian mechanism is not sufficient to raise the fluid temperature. It had confirmed by the temperature stability of samples x=0.3, 0.4 and 0.5 as shown in Fig.8. The major role in the heating mechanism is achieved by Néel relaxation.

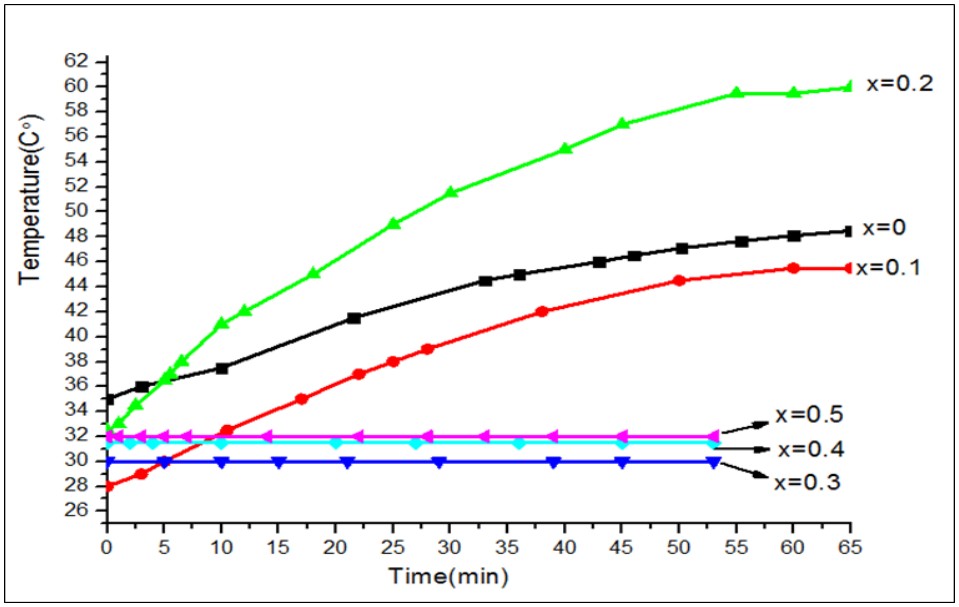

Figure.8: Heating curves water-based colloidal dispersions of the $Mn_{1-x}Zn_xFe_2O_4$ samples under a magnetic field of 6.5 kA/m and frequency 190 kHz.

5.3- The effective relaxation time and Néel relaxation time calculations.

An innovative mathematical approach had applied to calculate effective relaxation time and Néel relaxation time. Expresses on the power dissipation of a ferrofluid by the mathematical formula:

$$p = C_{P.nf}\frac{\Delta T}{\Delta t} \qquad (22)$$

Where $C_{P.nf}$(J/K) is the heat capacity of nanofluids. $\frac{\Delta T}{\Delta t}$ (K/s) represents corrected heating rate by Box- Lucas equation.

Imaginary part of susceptibility is measure of power dissipation i.e. $x'' = \frac{p}{\pi\mu_\circ f H^2}$ (Eq.12).By rewriting Eq.14b as following:

$\frac{x''}{x_\circ} = \frac{2\pi f\tau}{1+(2\pi f\tau)^2}$, let $\frac{x_\circ}{x''} = c$ and $y = 2\pi f\tau$ this leads to:

$$y^2 - cy + 1 = 0 \qquad (23)$$

Solving the equation by using the quadratic formula resulted in:

$$y = \frac{1}{2}\left(c - \sqrt{c^2 - 4}\right) \qquad (24)$$

Where $c = \frac{x_\circ}{x''} = \frac{\pi\mu_0^2 M_S^2 V f H^2}{3KT\, p}$ (25)

From the given c-value which can be obtained from experimental results; $y -$ have been solved and hence effective relaxation time (τ) were obtained, therefor $\tau_N$can be calculated from Eq.17.

SAR, $x_\circ, x', x'', \tau, \tau_N$and τ_B had calculated under magnetic field strength 6.5kA/m and the frequency 190kHz. As well as $C_{P.nf}$. The results are outlined in the following table:

Table 4: SAR values and superparamagnetic properties of ferrofluid samples x=0, 0.1and 0.2, which had generated heat under the alternating magnetic field H=6.5 kA/m and f=190 kHz.

Samples (x)	SAR (W/g)	$C_{P.nf}$ (J/g.K)	$\frac{\Delta T}{\Delta t}$ (K/s)	$x_\circ$	x'	x''	$\tau_{(s)}$	$\tau_{N(s)}$	τ_B (s)
0.0	8.316	4.0402	0.098	0.0142	2.834×10^{-3}	1.31×10^{-7}	1.6753×10^{-6}	1.437×10^{-5}	1.896×10^{-6}
0.1	5.775	4.053	0.068	3.093×10^{-3}	6.185×10^{-4}	9.13×10^{-8}	1.6753×10^{-6}	1.437×10^{-5}	1.896×10^{-6}
0.2	7.56	4.052	0.089	6.45×10^{-5}	1.288×10^{-5}	1.19×10^{-7}	1.676×10^{-6}	1.45×10^{-5}	1.896×10^{-6}

Standard sapphire method was used to calculate the specific heat capacity (C_P) of $Mn_{1-x}Zn_xFe_2O_4$ nanoparticles. From the obtained data; heat flow through samples and reference (sapphire) which had measured by using differential scanning calorimetry (DSC Q600), C_P were determined [51]. Fig.8 shows specific heat versus temperature.

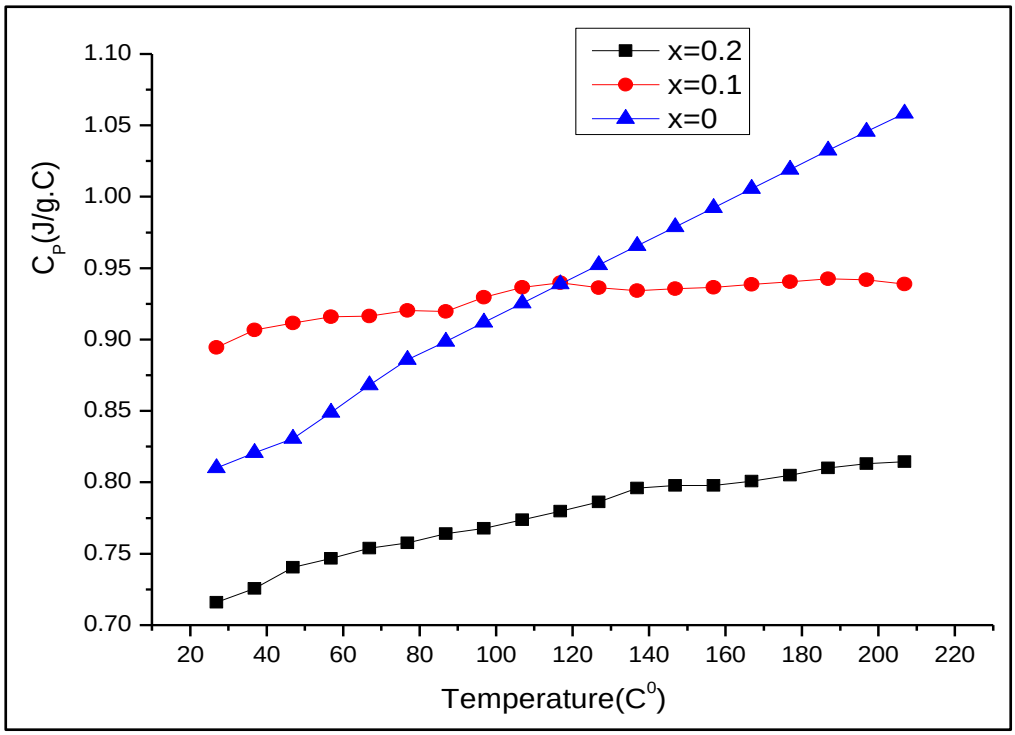

Figure.8: specific heat capacity as a function of temperature.

6. Conclusions

Synthesizes of $Mn_{1-x}Zn_xFe_2O_4$ nanoparticles were prepared by the coprecipitation method and followed by heat treatment by using an autoclave reactor. X-ray analysis showed that the presence undesired other structure in the composition before heat treatment. FESEM images confirmed the formation of the spherical shape nanostructure with the average particle size of about 20nm, and there is a slight change in the size of particles after heat treatment by the hydrothermal autoclave reactor. Hysteresis Loop curves manifest superparamagnetic behavior for prepared samples at room temperature. The heating ability of superparamagnetic nanoparticles had fulfilled by using an induction heater at a safe range for biomedical applications. The results showed that no heat released from the nanoparticles when the zinc content increased to 0.3 or more. As well as an unusual approach had utilized to calculate effective relaxation time (τ) and Néel relaxation time (τ_N).

References

[1] Jordan, A., Wust, P., Fählin, H., John, W., Hinz, A., & Felix, R, Inductive heating of ferrimagnetic particles and magnetic fluids: physical evaluation of their potential for hyperthermia, International journal of hyperthermia. 9 (1993) 51-68.

[2] Kwon, Y. S., Sim, K., Seo, T., Lee, J. K., Kwon, Y., & Yoon, T. J, Optimization of magnetic hyperthermia effect for breast cancer stem cell therapy, RSC advances. 6 (2016) 107298-107304.

[3] Chen, P., Cui, B., Cui, X., Zhao, W., Bu, Y., & Wang, Y,A microwave-triggered controllable drug delivery system based on hollow-mesoporous cobalt ferrite magnetic nanoparticles, Journal of Alloys and Compounds. 699 (2017) 526-533.

[4] R. C.O'handley, Modern magnetic materials: principles and applications, first ed., John Wiley&Sons,NewYork, (1999).

[5] M. Penchal Reddy, X. B. Zhou, Q. Huang, R. Ramakrishna Reddy, Synthesis and Characterization of Ultrafine and Porous Structure of Magnesium Ferrite Nanospheres, International Journal of Nano Studies & Technology. 3 (2014) 1-6.

[6] S.G. Jimeno, R.O. Palacios, M.C. Rubio, A. Vera, L. Leija, J. Estelrich, Improved thermal ablation efficacy using magnetic nanoparticles: a study in tumor phantoms, Prog. Electromagn. Res. 128 (2012) 229-248.

[7] J. Xie, C. Yan, Y. Yan, L. Chen, L. Song, F. Zang, Y. An, G. Teng, N. Gu, Y. Zhang, Multi-modal Mn-Zn ferrite nanocrystals for magnetically-induced cancer targeted hyperthermia: a comparison of passive and active targeting effects, Nanoscale. 8 (2016) 16902-16915.

[8] S.V. Jadhav , B.M. Kim , H.Y. Lee , I.C. Im , A.A. Rokade , S.S. Park , M.P. Patil ,G.D. Kim , Y.S. Yu , S.H. Lee, Induction heating and in vitro cytotoxicity studies of $MnZnFe_2O_4$ nanoparticles for self-controlled magnetic particle hyperthermia, Journal of Alloys and Compounds. 745 (2018) 282-291.

[9] K. Zhang, T. Holloway, J. Pradhan, M. Bahoura, R. Bah, R. R. Rakhimov, A. K. Pradhan, R. Prabakaran, and G. T. Ramesh,Synthesis and Magnetic Characterizations of $La_{1-x}Sr_xMnO_3$ Nanoparticles for Biomedical Applications, Journal of Nanoscience and Nanotechnology.pages.10 (2010) 5520–5526.

[10] M.Aneja, A.Tovstolytkin and G.S.Lotey, Superparamagnetic $LaSrMnO_3$ nanoparticles for magnetic nanohyperthermia and their biocompatibility, Journal of Magnetism and Magnetic Materials . 442 (2017) 423–428.

[11] Ihab Obaidat, Bashar Issa1,Virendra Mohiteand Yousef Haik, Controlling the Curie-temperature of Magnetic Nanoparticles for Hyperthermia, Dynamic Biochemistry, Process Biotechnology and Molecular Biology. 5 (2011) 85-88.

[12] Y. Qu, J. Li, J. Ren, J. Leng, C. Lin, D. Shi, Enhanced magnetic fluid hyperthermia by micellar magnetic nanoclusters composed of $Mn_xZn_{1-x}Fe_2O_4$ nanoparticles for induced tumor cell apoptosis, ACS applied materials & interfaces . 6 (2014) 16867-16879.

[13] William J Atkinson, Ivan A Brezovich, and Dev P Chakraborty. Usable frequencies in hyperthermia with thermal seeds. IEEE Transactions on Biomedical Engineering. BME-31 (1984) 70-75.

[14] S.A. Novopashin, M.A. Serebryakova, and S.Ya. Khmel, Methods of magnetic fluid synthesis (review), Thermophysics and Aeromechanics. 22 (2015) 397-412.

[15] Milanović, M., Stijepović, I., Pavlović, V., & Srdić, V. V, Functionalization of zinc ferrite nanoparticles: Influence of modification procedure on colloidal stability, Processing and Application of Ceramics. 10 (2016) 287-293.

[16] Ali M. M. , Sabah M.A.R. and Tahseen H.M., Dielectric Properties Of Cr-Substituted Cobalt Ferrite Nanoparticles Syntheses by Citrate-Gel Auto Combustion Method ,International Journal Of Applied Engineering Research.13 (2018) 6026-6035.

[17] K. M. Samb-Joshi , Y. A. Sethi , A. A. Ambalkar , H.B. Sonawane , S. P. Rasale, R. P. Panmand , R. Patil , B. B. Kale , and M.G. Chaskar, Lignin-Mediated Biosynthesis of ZnO and TiO_2 Nanocomposites for Enhanced Antimicrobial Activity, Journal of Composites Science. 3 (2019) 1-13.

[18] J. Smit, H. P. J. Wijn, Ferrites: Physical Properties of Ferrimagnetic Oxides in Relation to Their Technical Applications, Philips, N. V., Ed, Wiley, Eindhoven, Netherlands, 1959.

[19] K.J.Standley ,Oxide Magnetic Materials , second edition, Oxfored university, London, 1962.

[20] L. Kumar, P.Kumar, A. Narayan and M. Kar, Rietveld analysis of XRD patterns of different sizes of nanocrystalline cobalt ferrite, International Nano Letters, 3 (2013) 1-12.

[21] R.D. Shannon, Revised effective ionic radii and systematic studies of interatomic distances in halides and chalcogenides, Acta crystallographica section A: crystal physics, diffraction, theoretical and general crystallography. 32 (1976) 751-767.

[22] T.R. Tatarchuk , M. Bououdina , N.D. Paliychuk , I.P. Yaremiy , V.V. Moklyak, Structural characterization and antistructure modeling of cobalt substituted zinc ferrites, Journal of Alloys and Compounds,pp. 694 (2017) 777-791

[23] S.M. Patange, S.E. Shirsath, S.S. Jadhav, and K.M. Jadhav, Cation distribution study of nanocrystalline $NiFe_{2-x}Cr_xO_4$ ferrite by XRD, magnetization and Mössbauer spectroscopy, Phys. Status Solidi A, 209 (2012) 347–352.

[24] B. D. Cullity, C. D. Graham ,Introduction To Magnetic Materials, Second edition, Wiley-IEEE Press., Hoboken, New Jersey ,2009.

[25] M.Satalkar, S .N. Kane, On the study of Structural properties and Cation distribution of $Zn_{0.75-x}Ni_xMg_{0.15}Cu_{0.1}Fe_2O_4$ nano ferrite: Effect of Ni addition, Journal of Physics: Conference Series. 755 (2016) 012050.

[26] Mahmoud Goodarz Naseri and Elias B. Saion, Crystalization in Spinel Ferrite Nanoparticles, Advances in Crystallization Processes, in: Yitzhak Mastai (Ed.), InTech, 2012, pp.350-380

[27] Waqar Ahmed,Mark J. Jackson, Emerging nanotechnologies for manufacturing, Micro and Nanotechnology Series, second Edition. Elsevier, London, pp.485, (2015).

[28] R.D. Waldron, Infrared spectra of ferrites, Physical Review. 99 (1955) 1727-1735.

[29] K. V. Chandekar, K. M. Kant, Synthesis and characterization of low temperature superparamagnetic cobalt ferrite nanoparticles, Advanced Materials Letters.8 (2017) 435-443.

[30] T.R. Tatarchuk , M. Bououdina, N.D. Paliychuk , I.P. Yaremiy , V.V. Moklyak, Structural characterization and antistructure modeling of cobalt-substituted zinc ferrites, Journal of Alloys and Compounds, 694 (2017) 777-791.

[31] K.Nejati and R.Zabihi, Preparation and magnetic properties of nano size nickel ferrite particles using hydrothermal method, Chemistry Central Journal. 6 (2012) 1-6.

[32] S. Bedanta and W. Kleemann, Supermagnetism, Journal of Physics D: Applied Physics.42 (2009) 1-28.

[33] Tatarchuk, T., Bououdina, M., Vijaya, J. J., & Kennedy, L. J, Spinel ferrite nanoparticles: synthesis, crystal structure, properties, and perspective applications. In International Conference on Nanotechnology and Nanomaterials, Springer, Cham, 195 (2016) 305-325.

[34] H. Kavas , A. Baykal, Muhammet S. T, Y. Köseoğlu, M. Sertkol a, B. Aktaş, Cation distribution and magnetic properties of Zn doped $NiFe_2O_4$ nanoparticles synthesized by PEG-assisted hydrothermal route, Journal of Alloys and Compounds, 479 (2009) 49–55.

[35] H. Hauser, D.C. Jiles, Y. Melikhov, L. Li, R. Grössinger, An approach to modeling the dependence of magnetization on magnetic field in the high field regime, Journal of Magnetism and Magnetic Materials.300 (2006) 273–283

[36] S. .H. Mahmood, A. Awadallah, Y.Maswadeh, I. Bsoul, Structural and magnetic properties of Cu–V substituted M-type barium hexaferrites, International Conference on Advanced Materials,92 (2015) 1-24.

[37] H. Jalili, B. Aslibeiki, Ali G. Varzaneh and Volodymyr A. C, The effect of magneto-crystalline anisotropy on the properties of hard and soft magnetic ferrite nanoparticles, Beilstein Journal of Nanotechnology. 10 (2019) 1348–1359.

[38] K. M. Krishnan, Biomedical Nanomagnetics: A Spin Through Possibilities in Imaging, Diagnostics, and Therapy, IEEE Transactions on Magnetics. 46 (2010) 2523–2558.

[39] B.Mehdaoui , Anca Meffre , Julian Carrey , Sébastien Lachaize , Lise-Marie Lacroix , M. Gougeon , B.Chaudret , and M. Respaud, Optimal Size of Nanoparticles for Magnetic Hyperthermia: A Combined Theoretical and Experimental Study, Advanced Functionl Materials. 21(2011) 4573–4581.

[40] R.E. Rosensweig, Heating magnetic fluid with alternating magnetic field, Journal of Magnetism and Magnetic Materials. 252 (2002) 370–374.

[41] Kai Wu, Diqing Su, Jinming Liu, Renata Saha,, and Jian-Ping Wang, Magnetic Nanoparticles in Nanomedicine: A Review of Recent Advances, NANO-122164.R2 (2019),pp.1-95.

[42] G Schinteie, P Palade, L Vekas, N Iacob, C Bartha and V Kuncser, Volume fraction dependent magnetic behaviour of ferrofluids for rotating seal applications, Journal of Physics D Applied Ahysics. 46 (2013) 395501 (pp.1- 8).

[43] Alison E Deatsch and Benjamin A Evans. Heating efficiency in magnetic nanoparticle hyperthermia. Journal of Magnetism and Magnetic Materials.354 (2014) 163-172.

[44] Kestin, Joseph, Sokolov, Mordechai, Wakeham and William A, Viscosity of liquid water in the range −8 °C to 150 °C, Journal of Physical and Chemical Reference Data. 7(1978) 941-948.

[45] Cindi L. Dennis & Robert Ivkov, Physics of heat generation using magnetic nanoparticles for hyperthermia, International journal of Hyperthermia. 29 (2013) 715–729.

[46] R.R Wildeboer, P Southern, and QA Pankhurst, On the reliable measurement of specific absorption rates and intrinsic loss parameters in magnetic hyperthermia materials, Journal of Physics D: Applied Physics. 47 (2014) 495003 (pp.1- 4).

[47] D. E. Bordelon, C.Cornejo, C. Grüttner, F. Westphal, T.L. DeWeese, and R.Ivkov, Magnetic nanoparticle heating efficiency reveals magneto-structural differences when characterized with wide ranging and high amplitude alternating magnetic fields, Journal of Applied Physics. 109 (2011) 124904 (pp.1- 8).

[48] Sheng-Qi Zhou, and Rui Ni, Measurement of the specific heat capacity of water-based Al_2O_3 nanofluid, Applied Physics Letters. 92 (2009) 093123(pp.3)

[49] Harry O'Hanley, Jacopo Buongiorno, ThomasMcKrell, and Lin-wen Hu, Measurement and Model Validation of Nanofluid Specific Heat Capacity with Differential Scanning Calorimetry, Advances in Mechanical Engineering, Hindawi Publishing Corporation, Article ID 181079 ,2012, 6 pages.

[50] P. Madhu, P. G. Rajasekhar, Measurement of Density and Specific Heat Capacity of Different Nanofluids, International Journal of Advance Research, Ideas and Innovations in Technology.3 (2017) 165-170.

[51] Mathieu Lasfargues, Nitrate based High Temperature Nano-Heat-Transfer-Fluids: Formulation & Characterisation, thesis, The University of Leeds Institute of Particle Science & Engineering (IPSE), 2014,pp.52-60.